Residual Stresses in a Wire and Arc-Directed Energy-Deposited Al–6Cu–Mn (ER2319) Alloy Determined by Energy-Dispersive High-Energy X-ray Diffraction

T. KLEIN, P. SPOERK-ERDELY, C. SCHNEIDER-BROESKAMP, J.P. OLIVEIRA, and G. ABREU FARIA

In order to enable and promote the adoption of novel material processing technologies, a comprehensive understanding of the residual stresses present in structural components is required. The intrinsically high energy input and complex thermal cycle during arc-based additive manufacturing typically translate into non-negligible residual stresses. This study focuses on the quantitative evaluation of residual stresses in an Al–6Cu–Mn alloy fabricated by wire and arc-directed energy deposition. Thin, single-track aluminum specimens that differ in their respective height are investigated by means of energy-dispersive high-energy X-ray diffraction. The aim is to assess the build-up of stresses upon consecutive layer deposition. Stresses are evaluated along the specimen build direction as well as with respect to the lateral position within the component. The residual stress evolution suggests that the most critical region of the specimen is close to the substrate, where high tensile stresses close to the material's yield strength prevail. The presence of these stresses is due to the most pronounced thermal gradients and mechanical constraints in this region.

I. INTRODUCTION

ADDITIVE manufacturing (AM) processes use a localized heat source resulting in melting, solidification and consolidation of feedstock material usually in the form of powders or wires.[1] The prevailing complex temperature distribution and its temporal evolution, which involves pronounced thermal gradients and mechanical constraint-induced thermal strains during heating and cooling, result in residual stresses.[2,3] In large-scale metal AM processes,[4] such as wire and arc-directed energy deposition (waDED), these stresses can be in the magnitude of the material yield strength and oftentimes result in undesirable distortions[5] or cracking. Moreover, the residual stress state will have an impact on the mechanical properties and performance of the fabricated component.[6]

While the majority of reports on residual stresses in AM still focuses on structures fabricated by means of powder-bed based processes,[7–11] only selected studies have already taken up the complex topic of residual stress formation during waDED, as summarized, e.g., in recent reviews by Williams et al.[12] and Barath Kumar and Manikandan.[13] Besides being analyzed through various simulation approaches,[2,14,15] residual stresses are also determined experimentally, e.g., by means of neutron diffraction,[16–20] X-ray diffraction,[5,21,22] the contour method,[23] and the hole drilling method.[24] In the early work by Ding et al.,[19] for example, the thermo-mechanical behavior of multi-layer wall structures has been investigated, with the aim to describe how waDED components are affected by residual stresses and distortion. While the stress across the deposited walls was described as rather uniform, unclamping the substrate was found to lead to a significant stress redistribution, with a much lower stress value at the top of the wall than at the interface with the substrate. Findings published by Colegrove et al.[16] and Köhler et al.[21] later underscored this result, adding that in the

T. KLEIN and C. SCHNEIDER-BROESKAMP are with the LKR Light Metals Technologies, AIT Austrian Institute of Technology, 5282 Ranshofen, Austria. Contact e-mail: thomas.klein@ait.ac.at P. SPOERK-ERDELY is with the Department of Materials Science, Montanuniversität Leoben, 8700 Leoben, Austria and Institute of Materials Science, Joining and Forming, Graz University of Technology, 8010 Graz, Austria. J.P. OLIVEIRA is with the CENIMAT/I3N, Department of Materials Science, NOVA School of Science and Technology, Universidade NOVA de Lisboa, 2829-516 Caparica, Portugal. G. ABREU FARIA is with the Helmholtz-Zentrum Hereon, Institute of Materials Physics, 21502 Geesthacht, Germany.

top layer of wall structures even longitudinal compressive stresses can develop. This phenomenon appears to be a peculiarity of the waDED process, since it stands in contrast to many findings on the residual stresses developed during welding or laser powder-bed fusion.[2] Sun *et al.*[2] attempted to explain this behavior by comparing the restraint conditions in the different welding and AM processes: in the case of waDED, the degree of restraint decreases with the addition of filler wire, as opposed to the case of welding, and remains, compared to laser powder-bed fusion, at a lower level. Longitudinal residual stresses in waDED structures were in general found to be highest when compared to the residual stresses in the transverse and axial directions.[24] More recently, investigations have concentrated on the influences of certain parameters, such as deposition strategies,[18,23,25] component height,[2] or variations in the filler material,[21] often combining experimental and simulation approaches by means of finite element analysis. Other shapes besides walls, such as circular components,[24] have also been studied recently.

waDED parts can suffer from significant residual stresses and distortion. As a result, certain alleviating measures have also been investigated. Colegrove *et al.*,[16] Martina *et al.*,[26] and Hönnige *et al.*,[27] for example, studied the effect of interpass rolling on the residual stresses in waDED parts, since interpass rolling has been proposed to induce significant compressive residual stresses.[12] Colegrove *et al.*[16] found that particularly the large residual stresses close to the baseplate could be reduced. Furthermore, rolling may lead to a grain refinement of the waDED microstructure[16] and eliminate strong crystallographic texture as found, *e.g.*, in Ti alloys.[28] Pursuing alternative approaches, Sun *et al.*[29] investigated the influence of laser shock peening as a surface treatment on the residual stress state and tensile properties of waDED parts, while Ahmad *et al.*[23] studied the impact of hammer peening, and Duarte *et al.*[30] focused on a hot forging procedure integrated into the depostion technology. Shen *et al.*[20] and Hönnige *et al.*[28] also investigated the effect of post-production heat treatments.

A refined microstructure has a positive effect on the material's properties, but may also significantly facilitate the experimental determination of the residual stresses in AM materials. Coarse grains in relation to the measured gauge volume, such as often present in waDED structures, may introduce uncertainties in the experimental results.[16,27] In this context, Shen *et al.*[20] proposed the application of certain averaging methods during the experimental setup and processing of neutron diffraction data. Columnar grain growth and crystallographic texture may furthermore complicate the selection of appropriate diffraction elastic constants and require the introduction of stress factors.[11] In their recent reports on *in-situ* high-energy X-ray diffraction experiments during the deposition of 308L stainless steel wire onto 304L stainless steel substrate, Brown *et al.*[22,31] critically discuss the opportunities as well as experimental limitations in the determination of

inherently statistical parameters, including phase strains, residual stresses, and stress tensors. Since it is complex, expensive, and time-consuming to measure residual stresses, the body of literature on residual stresses in waDED components still lacks reliable studies that target further important processing parameters, reach out to further material classes by taking into account their microstructural peculiarities, and, most importantly, help to establish a sound understanding of the root causes for residual stress formation during waDED.[2,24]

In this work, we report on the evolution of the residual stress distribution in aluminum Al–6Cu–Mn (ER2319) wall structures fabricated by means of waDED. ER2319 belongs to the group of high-performance 2xxx alloys and has been proven to be processible by waDED.[32–34] No post-waDED processing such as heat treatment or deformation steps including rolling[16,17] or forging[30] have been performed. Specifically, in this work, we focus on the following: (i) the effects triggered by the consecutive layer additions through the use of equivalently processed specimens differing in their height only and (ii) the effects of specimen edges. For these analyses, energy-dispersive high-energy X-ray diffraction (HEXRD) is used. The obtained quantitative results showcase the build-up of substantial tensile residual stresses during deposition, especially close to the substrate. The observed levels of residual stress may subsequently result in the need for residual stress remedial actions during or after fabrication of waDED structures.

II. MATERIALS AND METHODS

A. *Alloy Composition and Processing*

An ABB IRB 4600-45/2.05 IRC5 robot equipped with a tilting rotary table and a Fronius CMT Advanced 4000R + VR 7000-CMT 4R/G/W/F + + power supply was used for waDED. An image of this setup is available in Supplementary Figure S1. A commercial cold metal transfer (CMT) current source was used for the experiments with Argon 5.0 as shielding gas. This combination is known to work well for waDED of 2xxx aluminum alloys.[35] The detailed parameters for waDED processing are provided in Table I.

The deposits were manufactured continuously without an interlayer waiting period. The deposition rate (DR) was estimated according to Eq. [1][36]:

Table I. Processing Parameters for waDED

Designation	Value	Unit
Wire Diameter	1.2	mm
Mean Wire Feed Rate	4.2	mm/min
Mean Voltage	10.3–11.0	V
Mean Current	55–65	A
Deposition Rate, DR	0.81	kg/h
Travel Speed	9.0	mm/s
Argon 5.0 Flow Rate	14.0	l/min

$$DR = 60 \cdot \rho \cdot \bar{v}_{WF} \cdot A_{WW}, \qquad [1]$$

where ρ is the material density in kg/m^3, $\bar{v}_{WF}$ is the mean wire feed speed in m/min and A_{ww} is the welding wire cross-sectional area in m^2. The density of the investigated alloy is 2.84×10^3 kg/m^3, and the wire cross-section area is 1.13×10^{-6} m^2 (Ø 1.2 mm). An industrial ER2319 wire from Safra SpA was used as feedstock wire, and AA2024 sheets in O temper condition with 2 mm thickness were used as substrates. The chemical composition of the wire, as determined by optical emission spectroscopy (OES) with SPECTROMAXx 6 from SPECTRO Analytical Instruments, is given in Table II. A series of five wall-shaped specimens, one of which is shown as an example in Figure 1(a), was manufactured with equivalent deposition parameters and heights ranging from 20 to 36 mm in steps of 4 mm. Each deposited layer was approximately 2 mm in height.

Table II. Chemical Composition of the ER2319 Wire and the waDED Deposit in Weight Percent

	Al	Cu	Mn	Ti	Zr	V	Fe	Si
Wire	bal.	6.24	0.23	0.20	0.10	0.06	0.07	0.03
waDED Deposit	bal.	6.11	0.25	0.17	0.15	0.08	0.07	0.04
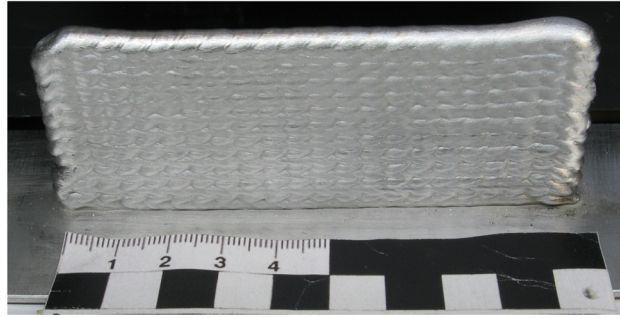
(a)
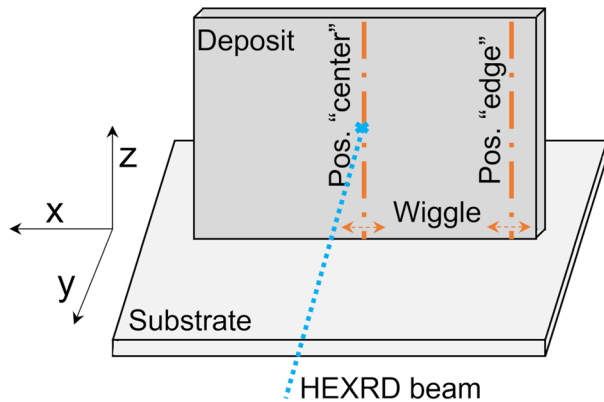
(b)

Fig. 1—(a) Exemplary photograph of a specimen (height 36 mm) with no visible surface defects or cracks; (b) schematic of the setup used for residual stress determination.

Thus, starting at a height of 20 mm, each consecutive sample was created by adding two more layers on a deposit manufactured equivalently to the previous one. We define the specimen coordinate system [Figure 1(b)] *via* the substrate plane as the x–y plane, with x corresponding to the welding direction and y to its orthogonal direction, and z as the build direction. The specimen thickness was approximately 5 mm with a typical layer roughness of 0.3 mm.

B. Microstructure and Mechanical Property Characterization

The deposits were characterized in terms of their solidification microstructure by means of optical light microscopy (OLM) using an Olympus BX60 microscope on metallographic cross-sections of the y–z plane polished with the Barker etchant. Scanning electron microscopy (SEM) was employed to analyze microsegregation resulting from solidification using a Tescan Mira 3 at 20 kV accelerating voltage in back-scattered electron (BSE) mode.

Hardness maps were recorded using a DuraScan 70 G5 microhardness tester from EMCO-TEST with a 100 g load, 10 seconds dwell time, and with 0.5 mm distance between indents in the y–z plane. Tensile tests were conducted using a Z100 testing machine from ZwickRoell GmbH & Co. KG. The tensile specimens with a gauge length of 10 mm, a width of 8 mm, and a thickness of 2.5 mm were tested according to EN-ISO 6892-1B. Specimens were extracted from waDED walls in x and in z directions.

C. Energy-Dispersive High-Energy X-ray Diffraction: Residual Stress Analysis

Diffraction measurements were made at the beamline P61A (White Beam Materials Science Beamline) at PETRA III at the Deutsches Elektronen-Synchrotron (DESY) in Hamburg, Germany. P61A delivers a high-intensity white beam with a continuous spectrum ranging from 20 to 200 keV. The diffraction signal is measured in energy-dispersive mode with an HPGe detector. The energy-dispersive diffraction geometry enables control of the diffracting gauge volume in the beam direction by defining a collimated incident and scattered beam path. The intersection between these two collimation paths defines the gauge volume, with a shape similar to a rhombic base prism.[37] The collimation of the scattered beam is done by the two sets of adjustable tungsten slits spaced by 500 mm, with one set directly in front of the detector. The detector is positioned at a distance of approximately 1335 mm from the gauge volume. The incident beam dimensions were 0.2×0.2 mm^2. The gauge volume length in the beam direction was determined by scanning a 100 μm tantalum foil in the beam direction and measuring the total intensity on the detectors. The resulting curve is a peak, with over 80 pct of the intensity resulting from a region within a length of 3 mm. The detector was positioned at a 2θ angle of 8.213 deg. Detector calibration was done with a Si powder sample (NIST 640f). For

each measurement, the gauge volume was positioned in the center of the walls with respect to the specimen thickness, with its longer direction aligned with the wall thickness. Measurements were performed at both, the specimens' centers and their edges. A scheme of the setup used is shown in Figure 1(b).

The goal of the experiment was to evaluate stresses in the wall plane in the x and z directions and assess their evolution with increasing wall height along the build direction (z). Although the solidification subgrain structure in the builds is small ($< 30~\mu$m), crystalline domains are still large (roughly 100 μm). This is due to the high number of low-angle grain boundaries in waDED materials,[38] in particular in the presence of grain refiners.[39] The result is a small grain population in the gauge volume, leading to granularity in the measured data and inducing high scatter on the computed stresses. To address this, stress evaluation was done using the $\sin^2\psi$ method,[40,41] where information from several directions is considered. Additionally, the samples were wiggled in a 10 mm range in the x direction perpendicular to the incident beam and the build direction. Along this direction, material deposition happens in a nearly steady-state fashion, so no significant stress variations are expected within the wiggling range. To ensure that the gauge volume at the edge position was still entirely inside the specimen, the center of the wiggling movement was positioned at > 5 mm off the physical edge. This measure is a tradeoff of the spatial resolution of edge-related effects and sufficient signal to omit granularity issues. A ψ-scan was done for each point across the height, with the ψ angle ranging from 0 to 90 deg with 5 deg steps, and 5 seconds exposure time. For each sample, ψ-scans were done from the substrate up to the upper edge of the wall with 0.5 mm steps. A ψ-scan is a sample rotation around the vector which bisects the incident and scattered beam vectors.[41] On the measurements presented, the value of ψ is the angle between σ_z and the diffraction vector. Across all measurements, only the α-aluminum matrix ($Fm\bar{3}m$) and Θ phases ($i4/mcm$) were observed.

A comb-shaped d_0 sample was fabricated from a similarly built ER2319 wall. The geometry of the sample is shown schematically in Supplementary Figure S2. The comb was produced by means of electron discharge machining. First, a 2 mm thick section of the wall cut in the y–z plane was sliced perpendicular to x. Afterward, teeth with a 2 mm spacing were produced along z direction by introducing 3 mm deep cuts in y direction. d_0 measurements were performed on each tooth from the build plate up to a height z of 50 mm. The d_0 sample also presented high granularity, but due to its geometry, wiggling on the x direction was not possible. Instead, measurements were made at several points inside each tooth, while the ψ axis was wiggled from 0 to 10 deg. d_0 was determined as the average of all measured values within each tooth. The calculated lattice parameter from the measured 420 peaks as well as their average per tooth and associated standard deviation is shown up to 20 mm from the build plate on Figure 2.

Figure 3 shows a representative diffraction pattern as obtained with the setup described. For each acquisition,
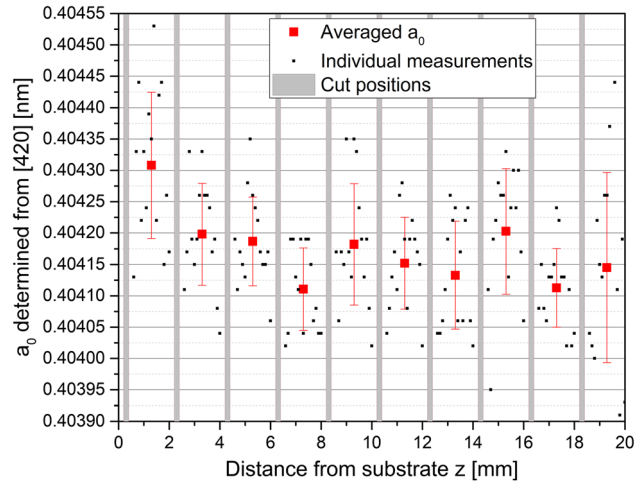

Fig. 2—Lattice parameter with respect to the distance from build plate for the reference d_0 specimen.

the 420 reflection and its surrounding peaks were fitted with pseudo-Voigt functions using a dedicated beamline software (P61A::Viewer[42]). Analysis focused on the 420 reflection due to its consistent intensity and low peak position variance across measurements, derived from its high multiplicity and low dependence on preferential orientation.[41] Fitted peak positions were used to calculate d-spacings, which were combined with the position-resolved d_0 values to produce strain vs $\sin^2\psi$ curves. A linear fit was done on the curves, and stresses were calculated using the diffraction elastic constants $s_1 = -5.148292 \times 10^{-6}~\text{MPa}^{-1}$ and $\frac{1}{2}s_2 = -6.19542116 \times 10^{-6}~\text{MPa}^{-1}$ obtained from Reference 43 accessed via the NIST ISODEC software.[44] For the computation, the normal stresses were evaluated in the coordinate system of the deposit as shown in Figure 1(b). Error bars were calculated based on the linear fit uncertainties following Reference 41.

III. RESULTS AND DISCUSSION

A. *Microstructure Characterization and Hardness*

The chemical compositions of the wire and deposit are compiled in Table II. There is no obvious evaporation of any of the alloying elements. The results of the basic microstructural characterization of the as-built 36 mm sample are shown in Figures 4(a) and (b). OLM [Figure 4(a)] demonstrates that the initially formed grain structure is very fine when using the CMT process for deposition. In all regions, except for the immediate vicinity of the substrate, equiaxed grains with mean sizes of 24.8 ± 1.1 μm dominate. This fine grain structure is seen as the result of the alloyed grain refining elements (Zr, Ti, and V) as well as the high cooling rates associated with the process.[45] Figure 4(b) visualizes the microstructure as observed by means of SEM. In the as-built material, characteristic microsegregation zones are visible. The pronounced BSE contrast suggests that they are predominantly due to the alloyed Cu, which

shows strong partitioning upon solidification in agreement with previously reported literature.[33,34]

Figure 4(c) details the hardness map of the y–z plane cross-section, where homogenous hardness values are observed except for the vicinity of the substrate. In the latter area, the microstructure locally varies due to increased cooling rates and intermixing with the substrate material, exerting a significant impact on the local material hardness. The higher hardness in the close vicinity of the substrate suggests that, in contrast to the as-deposited material far off the substrate, higher residual stresses could be accommodated in this region without distortion or relaxation. From a distance of roughly 5 mm from the substrate, the homogenous hardness values suggest that no interference with the observed residual stresses is to be expected.

B. Residual Stress Analysis

Figure 5 depicts the residual stresses σ_x and σ_z in the x and z directions, respectively, which were determined as a function of z position along the specimen height in the center of the 36 mm high as-built sample. Immediately above the substrate, pronounced tensile stresses prevail, because the shrinkage of the wall during cooling is restrained by the substrate (see Sun et al.[2]). The magnitude of the shrinkage in x direction induced by the first layer is larger than that induced by later layers, as the thermal gradient shows a maximum in this region.[23] The stress values in x direction are close to the yield strength of 100 to 110 MPa of non-heat-treated Al–6Cu–Mn, similar to values reported in Reference 46. The stresses decrease with increasing distance from the substrate, which is in agreement with the results of References 2 and 17. The high stresses in comparison withthe material yield strength result in distortions visible when unclamping the substrate plate. In the region from 5 to 10 mm above the substrate, the stresses are close to zero as the mechanical constraint is reduced, and above this, compressive stresses are found. At
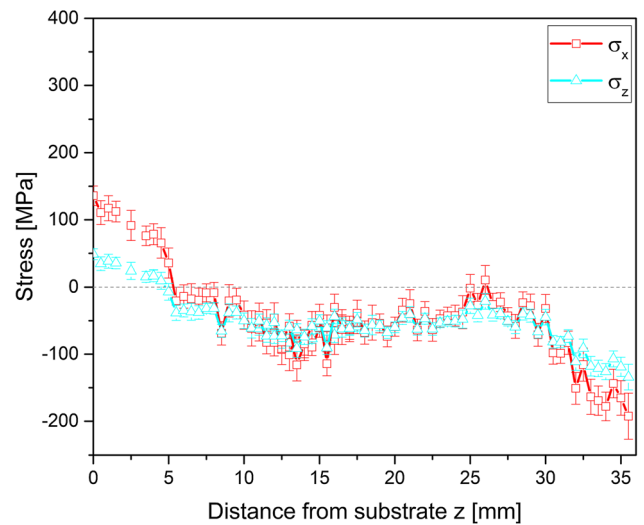

Fig. 3—HEXRD diffractogram with the peak positions of the phases present shown below. The 420 peak is indicated by an arrow, as it was used for further evaluation due to its low variation with texture.

Fig. 5—Comparison of the residual stress profiles in x and z directions as determined in the center of the 36 mm high specimen.
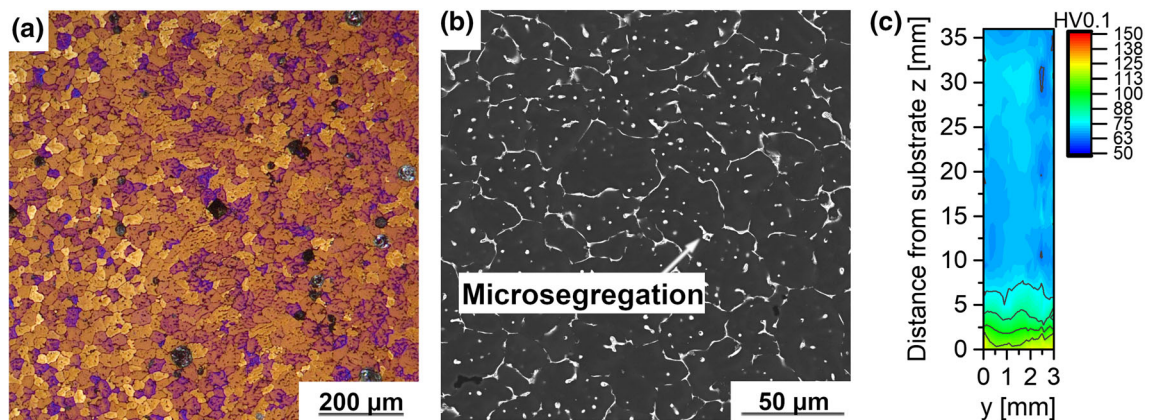

Fig. 4—Basic characterization of the as-built 36 mm specimen taken from a y–z cross-section at $z = 18$ mm. (a) OLM image showing a fine-grained structure with few pores (black dots); (b) SEM BSE image with clearly visible microsegregation zones; (c) Vickers hardness map of the y-z plane cross-section.

approximately 25 mm, the stresses are again close to zero, with their evolution qualitatively counterbalancing the tensile stresses at the bottom of the sample.

Both stresses in x and z directions qualitatively show the same trends regarding this local maximum roughly 10 mm below the top of the specimen, but the transversal stresses σ_x are higher in magnitude. The stress evolution simulated by Sun et al.[2] is in qualitative agreement with the present results. These authors suggested the origin of this stress progression to result from the intrinsic heat treatment. Also, qualitatively similar experimental data were obtained by Hönnige et al.[17] using neutron diffraction. However, in their work, the stresses were evaluated only up to certain z positions, but not along the samples' entire heights, whereby the particularities of the evolution of compressive stresses could not be monitored. Li et al.[24] and Doumenc et al.[18] observed a similar progression of stresses with respect to z, with stresses in x direction being of the highest magnitude. The latter authors admitted that this global trend among the stress directions, i.e., the trend regarding their similar progressions with respect to specimen height, has not found any comprehensive explanation so far.

Figures 6(a) and (b) depict the comparison of the residual stresses in x and z direction in the center and at the edge of the 20 mm specimen. Differences are most pronounced in the close vicinity of the substrate, where in the first layer, very high tensile stresses prevail. At the edge, these tensile stresses are in both cases significantly higher than in the center of the specimen (e.g., for σ_x: $\sigma_{x,\text{edge}} = 340$ vs. $\sigma_{x,\text{center}} = 250$ MPa). However, they decrease right after the first layer, falling quickly below the stress values measured in the center at the respective distances and are then close to null or in compressive condition. This effect may be due to the different cooling conditions in the center and at the edge of the fabricated component, which depend on the geometrically determined heat conduction conditions. This observation is qualitatively replicated by the simulations by Oyama et al.[47] It is noted that individual residual stress values above the (uniaxial) strength values of materials can occur as a result of the multi-axiality of the residual stress state.

The intermixing of deposited material and substrate can cause compositional gradients which affect the d-spacing and the stress computation in the first layer. The position-resolved d_0 measurement minimizes any errors resulting from this. However, as local differences in the intermixing compositional gradient can occur across samples, it has to be noted that the stress values determined in the first layer above the substrate may in fact be affected by intermixing between the deposited material (ER2319) and the substrate material (AA2024) to an unknown extent. Indeed, Figure 2 indicates an increase in d_0 toward the build plate, although the behavior within the first millimeter from the substrate could not be measured due to the electrical discharge machining cut. Additionally, variations between two consecutive data points are oftentimes observed, which are, to a large extent, a result of measurement uncertainty. Alternatively, this behavior may reflect the oscillating stress distribution that can be present in DED samples as originally shown by Strantza et al.,[48] which cannot be accurately resolved using the present experimental conditions, in particular, in terms of beam size and resultant spatial resolution in z direction.

Figures 7(a) and (b) visualize σ_x and σ_z for different deposit heights ≥ 24 mm as determined in the center position. The region in the close vicinity of the substrate is equivalent in all specimens. The pronounced tensile residual stresses do not seem to be relaxed by the intrinsic heat treatment induced during the process. It is therefore concluded that irrespective of the specimen height, countermeasures against the high tensile residual stresses are required, if the substrate is incorporated into the final structure or component. Such countermeasures
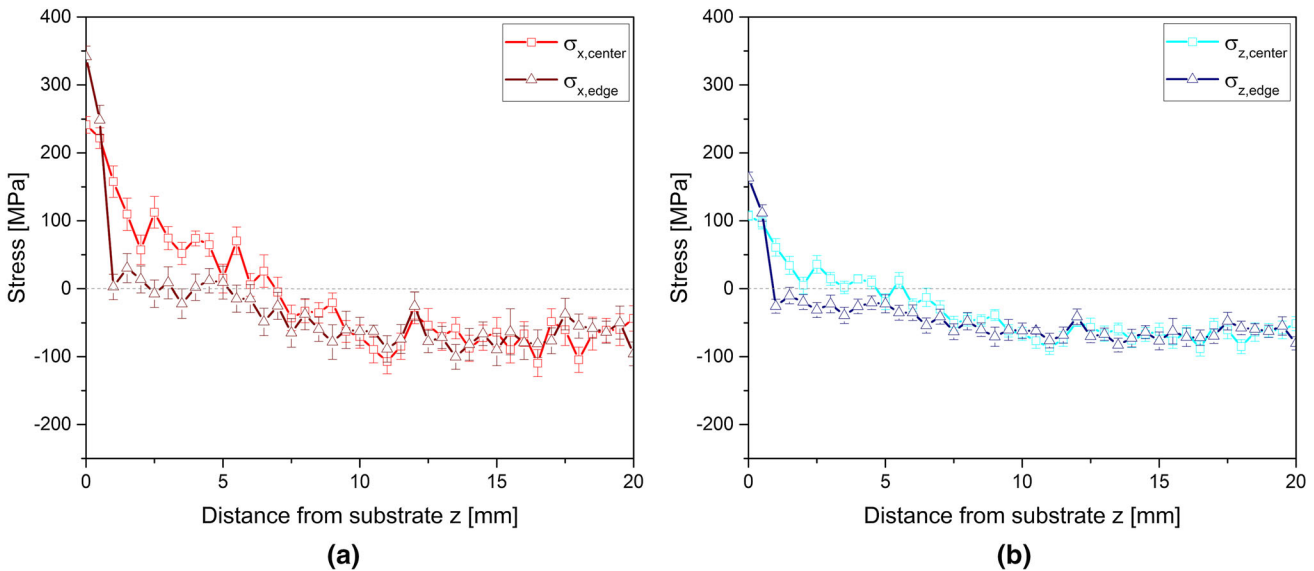

Fig. 6—Residual stress profiles for center and edge in (a) x and (b) z directions determined for the 20 mm specimen.
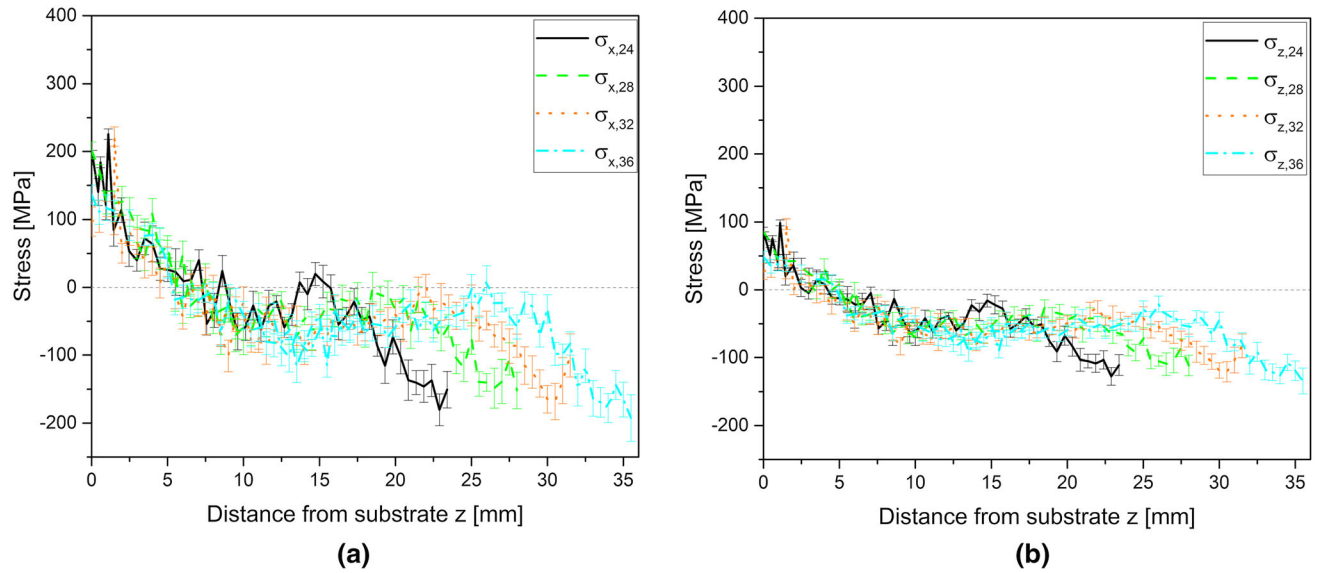
Fig. 7—Residual stress profiles of (*a*) σ_x and (*b*) σ_z as determined in the specimen center for various specimen heights.

can be hot working incorporated into the process[17] or post-process stress relief heat treatments.[20,28]

In the compressive region, the location of the local maximum is clearly dependent on the specimen height—a phenomenon equally prevalent in *x* and *z* directions. With increasing height, the maxima are slightly reduced, which can be argued to result from an increasing stiffness upon consecutive deposition of additional layers, which is in agreement with Reference 49. The location of the maximum itself can be rationalized for each specimen height, as it is located approximately 10 mm below the top of each specimen. The d_0 values determined do not reflect such a behavior up to the sample heights of 36 mm studied here and, therefore, effects of Cu concentration variations can be excluded. Such local stress maxima are not expected in welded materials, where typically plateaus are observed in transversal direction, which extend into the far-field stresses of the structure or component. It has been suggested that this scenario can be a result of welding residual stresses superimposed with bending stresses arising from clamping of the substrate.[50,51] Assuming that the mechanical constraint exerted onto a waDED build by the clamped substrate replicates the mechanical constraint of a fusion weld fixed by the parts to be joined, the superposition of the stress fields seems to be the likely cause for the occurrence of the local maxima. However, fusion welding scenarios for joining applications may require different clamping geometries, which can influence the resultant superimposed stresses to an unknown extent. Using the contour method on stainless steel waDED builds, Huang *et al.*[3] have recently demonstrated a behavior very similar to the one we have observed. It is noted that in applications that require the removal of the substrate, the stress state will be affected dramatically.[23]

The residual stresses at the top of each sample are compressive in nature and of similar magnitude irrespective of the sample height. Non-negligible residual stresses may be caused by the mechanical constraint exerted by the already solidified and cooled layer beneath and the fact that the location of stress determination is not directly at the surface but slightly beneath, corresponding to the size of the probed volume. Non-negligible stresses close to the sample surface in *z* direction were in fact also observed by Doumenc *et al.*[18]

IV. SUMMARY AND CONCLUSIONS

The present work was performed to provide detailed and quantitative information about the residual stress state of an important aluminum alloy, Al–6Cu–Mn, after deposition by means of waDED. Based on the performed analyses, the major observations on residual stresses can be summarized as follows: (i) In the close vicinity of the substrate, high tensile stresses prevail in *x* and *z* directions. In the layers further away from the substrate, compressive stresses are active. The highest tensile stresses can reach the magnitude of the yield strength, which must be considered in the design of actual components manufactured by waDED; (ii) Stresses in *x* and *z* directions show similar profile shapes with respect to the specimen height, with stresses in *x* direction being higher in magnitude. The profile shapes can be rationalized as a result of the mechanical constraints during solidification and the ensuing cooling; (iii) At specimen edges, the region of high tensile stresses is restricted to the first layer only, whereas, in the center of the specimens, a corresponding decrease in residual stresses is completed just above a height of 5 mm; (iv) In all specimens, a characteristic local maximum is observed in the stress profiles approximately 10 mm below the top, which may be caused by superimposed welding stresses and bending stresses resulting from clamping of the substrate; (v) The residual stress analysis of the Al–6Cu–Mn alloy was

accompanied by microstructural and mechanical characterization, supporting the conclusions drawn from residual stress analyses and their interpretation.

In summary, non-negligible stresses are formed during waDED of a commercial ER2319 aluminum alloy that requires remedial actions for the future incorporation of such structures into applications. Future work will, hence, focus on the use of process modifications and/or heat treatments to reduce these process-induced undesirable stresses.

CONFLICT OF INTEREST

The authors declare that they have no known conflict of interest that could have appeared to influence the work reported in this paper.

OPEN ACCESS

REFERENCES

1. D. Herzog, V. Seyda, E. Wycisk, and C. Emmelmann: *Acta Mater.*, 2016, vol. 117, pp. 371–92.
2. J. Sun, J. Hensel, M. Köhler, and K. Dilger: *J. Manuf. Process.*, 2021, vol. 65, pp. 97–111.
3. W. Huang, Q. Wang, N. Ma, and H. Kitano: *J. Manuf. Process.*, 2022, vol. 82, pp. 434–47.
4. T. Lehmann, D. Rose, E. Ranjbar, M. Gasri-Khouzani, M. Tavakoli, H. Henein, T. Wolfe, and A.J. Qureshi: *Int. Mater. Rev.*, 2022, vol. 67, pp. 410–59.
5. K. Wandtke, D. Schroepfer, R. Scharf-Wildenhain, A. Haelsig, T. Kannengiesser, A. Kromm, and J. Hensel: *Weld. World*, 2023, vol. 67, pp. 987–96.
6. H. Lockett, J. Ding, S. Williams, and F. Martina: *J. Eng. Des.*, 2017, vol. 28, pp. 568–98.
7. Y. Liu, Y. Yang, and D. Wang: *Int. J. Adv. Manuf. Technol.*, 2016, vol. 87, pp. 647–56.
8. T. Simson, A. Emmel, A. Dwars, and J. Böhm: *Addit. Manuf.*, 2017, vol. 17, pp. 183–89.
9. W. Zhang, D. Guo, L. Wang, C.M. Davies, W. Mirihanage, M. Tong, and N.M. Harrison: *Addit. Manuf.*, 2023, vol. 61, p. 103275.
10. F. Schmeiser, E. Krohmer, N. Schell, E. Uhlmann, and W. Reimers: *Addit. Manuf.*, 2020, vol. 32, p. 101028.
11. J. Schröder, A. Evans, V. Luzin, G. Abreu Faria, S. Degener, E. Polatidis, J. Čapek, A. Kromm, G. Dovzhenko, and G. Bruno: *J. Appl. Crystallogr.*, 2023, vol. 56, pp. 1076–90.
12. S.W. Williams, F. Martina, A.C. Addison, J. Ding, G. Pardal, and P. Colegrove: *Mater. Sci. Technol.*, 2016, vol. 32, pp. 641–47.
13. M.D.B. Kumar and M. Manikandan: *Met. Mater. Int.*, 2022, vol. 28, pp. 3033–56.
14. C.T. Justus Panicker, K. Rohit Surya, and V. Senthilkumar: *Mater. Today Proc.*, 2022, vol. 59, pp. 1119–26.
15. H. Huang, N. Ma, J. Chen, Z. Feng, and H. Murakawa: *Addit. Manuf.*, 2020, vol. 34, p. 101248.
16. P.A. Colegrove, H.E. Coules, J. Fairman, F. Martina, T. Kashoob, H. Mamash, and L.D. Cozzolino: *J. Mater. Process. Technol.*, 2013, vol. 213, pp. 1782–91.
17. J.R. Hönnige, P.A. Colegrove, S. Ganguly, E. Eimer, S. Kabra, and S. Williams: *Addit. Manuf.*, 2018, vol. 22, pp. 775–83.
18. G. Doumenc, L. Couturier, B. Courant, P. Paillard, A. Benoit, E. Gautron, B. Girault, T. Pirling, S. Cabeza, and D. Gloaguen: *Materialia*, 2022, vol. 25, p. 101520.
19. J. Ding, P. Colegrove, J. Mehnen, S. Ganguly, P.M.S. Almeida, F. Wang, and S. Williams: *Comput. Mater. Sci.*, 2011, vol. 50, pp. 3315–22.
20. C. Shen, M. Reid, K.D. Liss, Z. Pan, Y. Ma, D. Cuiuri, S. van Duin, and H. Li: *Addit. Manuf.*, 2019, vol. 29, p. 100774.
21. M. Köhler, S. Fiebig, J. Hensel, and K. Dilger: *Metals (Basel)*, 2019, vol. 9, p. 608.
22. D.W. Brown, A. Losko, J.S. Carpenter, B. Clausen, J.C. Cooley, V. Livescu, P. Kenesei, J.S. Park, T.J. Stockman, and M. Strantza: *Metall. Mater. Trans. A*, 2020, vol. 51A, pp. 1379–94.
23. B. Ahmad, X. Zhang, H. Guo, M.E. Fitzpatrick, L.M.S.C. Neto, and S. Williams: *Metals (Basel)*, 2022, vol. 12, p. 253.
24. R. Li, J. Xiong, and Y. Lei: *J. Manuf. Process.*, 2019, vol. 40, pp. 59–67.
25. M.A. Somashekara, M. Naveenkumar, A. Kumar, C. Viswanath, and S. Simhambhatla: *Int. J. Adv. Manuf. Technol.*, 2017, vol. 90, pp. 2009–25.
26. F. Martina, M.J. Roy, B.A. Szost, S. Terzi, P.A. Colegrove, S.W. Williams, P.J. Withers, J. Meyer, and M. Hofmann: *Mater. Sci. Technol.*, 2016, vol. 32, pp. 1439–48.
27. J.R. Hönnige, P.A. Colegrove, B. Ahmad, M.E. Fitzpatrick, S. Ganguly, T.L. Lee, and S.W. Williams: *Mater. Des.*, 2018, vol. 150, pp. 193–205.

28. J. Hönnige, C.E. Seow, S. Ganguly, X. Xu, S. Cabeza, H. Coules, and S. Williams: *Mater. Sci. Eng. A*, 2021, vol. 801, p. 140368.
29. R. Sun, L. Li, Y. Zhu, W. Guo, P. Peng, B. Cong, J. Sun, Z. Che, B. Li, C. Guo, and L. Liu: *J. Alloys Compd.*, 2018, vol. 747, pp. 255–65.
30. V.R. Duarte, T.A. Rodrigues, N. Schell, R.M. Miranda, J.P. Oliveira, and T.G. Santos: *Addit. Manuf.*, 2020, vol. 35, p. 101193.
31. D.W. Brown, A. Losko, J.S. Carpenter, J.C. Cooley, B. Clausen, J. Dahal, P. Kenesei, and J.S. Park: *Metall. Mater. Trans. A*, 2019, vol. 50A, pp. 2538–53.
32. E.M. Ryan, T.J. Sabin, J.F. Watts, and M.J. Whiting: *J. Mater. Process. Technol.*, 2018, vol. 262, pp. 577–84.
33. M. Arana, E. Ukar, I. Rodriguez, D. Aguilar, and P. Álvarez: *Mater. Des.*, 2022, vol. 221, p. 110974.
34. N. Mclean, M.J. Bermingham, P. Colegrove, A. Sales, and M.S. Dargusch: *Sci. Technol. Weld. Join.*, 2022, vol. 27, pp. 479–89.
35. M. Silmbroth, N. Enzinger, C. Schneider-Bröskamp, A. Arnoldt, and T. Klein: *Sci. Technol. Weld. Join.*, 2023, vol. 28, pp. 314–22.
36. E. Aldalur, F. Veiga, A. Suárez, J. Bilbao, and A. Lamikiz: *J. Manuf. Process.*, 2020, vol. 58, pp. 615–26.
37. R. Farla, S. Bhat, S. Sonntag, A. Chanyshev, S. Ma, T. Ishii, Z. Liu, A. Néri, N. Nishiyama, G.A. Faria, T. Wroblewski, H. Schulte-Schrepping, W. Drube, O. Seeck, and T. Katsura: *J. Synchrotron Radiat.*, 2022, vol. 29, pp. 409–23.
38. M. Froend, V. Ventzke, F. Dorn, N. Kashaev, B. Klusemann, and J. Enz: *Mater. Sci. Eng. A*, 2020, vol. 772, p. 138635.
39. L. Wang, Y. Suo, Z. Liang, D. Wang, and Q. Wang: *Mater. Lett.*, 2019, vol. 241, pp. 231–34.
40. E. Macherauch: *Exp. Mech.*, 1966, vol. 6, pp. 140–53.
41. V. Hauk: *Structural and Residual Stress Analysis by Nondestructive Methods: Evaluation—Application—Assessment: Section 2.072f*, Elsevier Science, Amsterdam, 1997.
42. P61A:: Viewer, https://hereon-gems.github.io/P61AToolkit/introduction.html#p61a-viewer. Accessed 28 Feb 2023.
43. R.F.S. Hearmon: *Adv. Phys.*, 1956, vol. 5, pp. 323–82.
44. T. Gnäupel-Herold: *J. Appl. Crystallogr.*, 2012, vol. 45, pp. 573–74.
45. T. Klein, G. Graf, P. Staron, A. Stark, H. Clemens, and P. Spoerk-Erdely: *Mater. Lett.*, 2021, vol. 303, p. 130500.
46. Z. Huang, J. Huang, X. Yu, G. Liu, and D. Fan: *J. Mater. Eng. Perform.*, 2023, vol. 32, pp. 1810–23.
47. K. Oyama, S. Diplas, M. M'hamdi, A.E. Gunnæs, and A.S. Azar: *Addit. Manuf.*, 2019, vol. 26, pp. 180–92.
48. M. Strantza, B. Vrancken, M.B. Prime, C.E. Truman, M. Rombouts, D.W. Brown, P. Guillaume, and D. Van Hemelrijck: *Acta Mater.*, 2019, vol. 168, pp. 299–308.
49. M.J. Benoit, S.D. Sun, M. Brandt, and M.A. Easton: *J. Manuf. Process.*, 2021, vol. 64, pp. 1484–92.
50. R.H. Leggatt: *Int. J. Press. Vessel. Pip.*, 2008, vol. 85, pp. 144–51.
51. B.A. Szost, S. Terzi, F. Martina, D. Boisselier, A. Prytuliak, T. Pirling, M. Hofmann, and D.J. Jarvis: *Mater. Des.*, 2016, vol. 89, pp. 559–67.